Chemistry & Biodiversity

WILEY-VCH

CHEMISTRY & BIODIVERSITY

RESEARCH ARTICLE OPEN ACCESS

Probing the Inhibitory Potential of Halogenated Symmetrical Formamidine Against MAO-A and MAO-B: Structural Elucidation, Molecular Dynamic Simulation and DFT Computational Studies

Segun D. Oladipo[1,2] | Robert C. Luckay[1] | Samuel O. Olalekan[3] | Abosede A. Badeji[4] | Tunde L. Yusuf[5] | Adesola A. Adeleke[2] | Nonkosi Matinise[1]

[1]Department of Chemistry and Polymer Science, Stellenbosch University, Matieland, South Africa | [2]Department of Chemical Sciences, Olabisi Onabanjo University, Ago-Iwoye, Nigeria | [3]Department of Physiology, Olabisi Onabanjo University, Sagamu, Nigeria | [4]Department of Chemical Sciences, Tai Solarin University of Education, Ijagun, Nigeria | [5]Department of Chemistry, Faculty of Natural and Agricultural Sciences, University of Pretoria, Hatfield, South Africa

Correspondence: Segun D. Oladipo (segun.oladipo@oouagoiwoye.edu.ng) | Robert C. Luckay (rcluckay@sun.ac.za)

Received: 12 March 2025 | **Revised:** 12 May 2025 | **Accepted:** 28 May 2025

Funding: This study was funded by National Research Foundation (grant number: CPRR23041794158).

Keywords: crystal structure | DFT | formamidine | MAO-A/B | Parkinson's disease

ABSTRACT

A halogenated symmetrical formamidine, *N*,*N*′-bis(3-chloro-4-fluorophenyl)formamidine (FCF) was synthesized by the condensation reaction between triethyl orthoformate and 3-chloro-4-fluoroaniline in 1:2 ratio. The compound FCF was characterized by FT-IR, mass, NMR (^{1}H and ^{13}C) spectroscopic techniques and the purity was confirmed by elemental analysis. Crystal structural elucidation of FCF showed that it conformed to an *E*-anti-molecular isomer. In the crystal packing system of FCF, there exists N—H···N hydrogen bonding intermolecular interactions between the azomethine nitrogen (N-azomethine) and amine hydrogen (H-amine) atoms of neighboring molecules resulting in the formation of dimers with an $R_2^2(8)$ graph set motif. Hirshfeld surface analysis unraveled that, H···H and Cl···H intermolecular contacts contributed equally and the most with each of them contributing 14.6% in crystal packing. The geometrical and electronic properties of FCF were investigated using DFT/B3LYP/6-311++G(d,p) basis sets. Mulliken and MESP analyses identified reactive sites, while FMO studies revealed a HOMO–LUMO gap (4.62 eV) indicative of intermediate reactivity and stability. Molecular docking and molecular dynamics simulations (MDS) were performed to evaluate the inhibitory potential of FCF against monoamine oxidase A (MAO-A) and monoamine oxidase B (MAO-B), both are protein targets for managing Parkinson's disease. Docking studies revealed that FCF exhibited superior binding affinity towards both MAO-A and MAO-B compared to the reference drugs (harmine and rasagiline) as reflected in its more negative docking scores. MDS analysis was conducted over 100 ns and we found out that FCF demonstrated superior inhibitory potential against MAO-A and MAO-B compared to the reference drugs, as indicated by its stronger binding free energies (-38.78 ± 2.62 kcal mol^{-1} for MAO-A and -34.15 ± 3.29 kcal mol^{-1} for MAO-B) relative to harmine (-32.43 ± 2.26 kcal mol^{-1}) and rasagiline (-32.44 ± 2.65 kcal mol^{-1}). Furthermore, MDS analysis also confirmed the stability of FCF–protein complexes, with lower RMSD values suggesting greater structural stability. In addition, pharmacokinetic analysis revealed that FCF possesses favorable drug-like properties, including high gastrointestinal absorption, blood–brain barrier permeability, and a nontoxic profile, reinforcing its potential as a promising therapeutic agent for targeting neurodegenerative disorders such as Parkinson's disease.

1 | Introduction

Parkinson's disease (PD) is a rapidly growing neurodegenerative disorder characterized by motor symptoms such as tremor, bradykinesia, and rigidity, as well as nonmotor symptoms including cognitive impairment, depression, and sleep disorders [1]. Its prevalence varies significantly across geographical regions, influenced by factors such as age distribution, environmental exposures, and healthcare accessibility. For example, studies in Latin America estimate a PD prevalence of 472 per 100 000 individuals, with higher rates among older populations and significant variations based on the source of data [2]. In Poland, a recent analysis identified an increase in PD prevalence over a decade, reaching 269 per 100 000 individuals, with a higher prevalence in women—a pattern distinct from most global trends [3]. Similarly, data from China revealed a prevalence of 1.86% among individuals aged 65 years and older, with risk factors such as pesticide exposure and urban residency contributing to the disease burden [4]. These findings underscore the global prevalence of PD and its predisposing factors.

PD is primarily associated with the degeneration of dopaminergic neurons in the substantia nigra, leading to decreased dopamine levels in the striatum [5]. The exact pathophysiological mechanisms remain complex, involving mitochondrial dysfunction, oxidative stress, and neuroinflammation [6]. A key feature of PD is the production of 3,4-dihydroxyphenylacetaldehyde (DOPAL), a toxic byproduct of dopamine metabolism by monoamine oxidase (MAO) [7]. DOPAL accumulation damages dopaminergic neurons, contributing to PD. Inhibiting monoamine oxidase B (MAO-B) reduces DOPAL production, offering neuroprotection and potentially slowing disease progression. MAO-B inhibitors like selegiline and rasagiline increase dopamine availability but may cause side effects, including headache and dizziness [8]. Thus, developing new compounds to inhibit MAO-B effectively with fewer side effects is crucial.

Formamidines are organic compounds which conform to general formula $R^1N{=}C(H)NHR^2$ and aryl as well as alkyl moieties are represented as either R^1 or R^2. Formamidines, especially the *N*,*N*′-diarylformamidines can be classified as either symmetrical (if $R^1 = R^2$) or unsymmetrical ($R^1 \neq R^2$). They have myriad applications such as ligands in coordination chemistry [9], monomeric units in building up of polymers [10], histamine receptor antagonists [11], pesticides [12], and metal complexes derived from formamidines have been widely reported to display certain biological activities [13–15]. In this study, *N*,*N*′-bis(3-chloro-4-fluorophenyl)formamidine (FCF) is synthesized and explored as a potential therapeutic in managing PD by examining its MAOs inhibitory potency using in silico approaches. The rationale behind this study was due to preliminary results obtained after searching for possible biomolecular targets for FCF using cohorts of cheminformatic tools, suggesting monoamine oxidase A (MAO-A) and MAO-B proteins as possible targets. Inhibiting these enzymes can help maintain higher dopamine levels, thus alleviating the symptoms of PD.

Literature has shown that some formamidine derivatives could inhibit MAO proteins. Benezet et al. [16], reported the ability of *N*′-(5-chloro-2,4-dimethoxyphenyl)-*N*,*N*-dimethylformamidine to inhibit rat brain MAO in vivo by exploring intraperitoneal injection. Likewise, *N*′-(4-chloro-o-tolyl)-*N*,*N*-dimethylformamidines have been reported to increase the dopamine's level in rat brain revealing its tendency to inhibit MAO [17]. These findings suggest that formamidine derivatives could potentially offer therapeutic benefits in neurodegenerative conditions like PD. Herein, we probe into the inhibitory potential of FCF against MAO-A and MAO-B, which might in turn unravel the therapeutic properties of FCF as a possible drug to manage Parkinson's and other neurodegenerative diseases.

2 | Experimental Section

2.1 | Reagents and solvents

All the solvents used for this research work are A.C.S grade (purity ≥ 99.5%) and they were purchased from Merck and used as obtained without purifying them further. The chemicals, 3-chloro-4-fluoroaniline (98%) and triethyl orthoformate (98%) were also sourced from Merck.

2.2 | Instrumentation

Bruker Avance III 600 MHz spectrometer was used to record the NMR spectra (^{1}H and ^{13}C) for FCF at 25°C. Deuterated dimethyl sulfoxide was utilized as a solvent to run the NMR analysis and peaks which were observed at δ 2.50 and δ 39.52 ppm are assigned to residual $(CD_3)_2SO$. The Nicolet avatar 330 FT-IR spectrometer coupled with ZnSe 1455 ATR was used to obtain the FT-IR spectrum of the FCF. A mass spectrum was obtained using Waters Synapt G2 coupled to Waters UPLC., ESI probe, ESI positive, cone voltage 15 V while the SMP20 melting point machine was used to determine the melting point.

2.3 | Preparation of FCF

The compound FCF was synthesized by following a reported protocol in the literature with a slight modification [14, 15]. In a 100 mL round bottom flask containing triethyl orthoformate (1 mmol), 3-chloro-4-fluoroaniline (2 mmol) was added. Three to four drops of glacial acetic was added to the resultant mixture in the bottom flask and the solution was stirred and refluxed within the range of 140°C–150°C for 30 min. A whitish compound crashed out of the solution and the mixture was distilled, to remove ethanol, which was the side-product of the reaction. The crude whitish product was thoroughly washed with hexane to remove unreacted 3-chloro-4-fluoroaniline and then filtered. The purified product was dried in an oven at 30°C and kept in an airtight desiccator for further spectroscopic analysis. Yield 77%. M.P.: 176°C–177°C. ^{1}H NMR ($CDCl_3$, 600 MHz) δ (ppm): 7.15 (s, 2H, Ar-H), 7.35 (t, 4H, $J_{H,H}$ = 9, Ar-H), 8.30 (s, 1H, —CH═N), 9.97 (s, 1H, —NH-Ar). ^{13}C NMR ($CDCl_3$, 150 MHz) δ (ppm): 117.34, 117.5, 119.9, 120.0, 121.1, 149.6, 152.8, 154.4 and 160.4. FT-IR (cm^{-1}) 3078, 2998, 1664, 1589, 1258, 1125, 886, and 759. ES-TOF MS: *m*/*z* (%): $[M]^+$, 301.0109, $[M+2]^+$, 303.0081, MS calc. analysis: 300.00 (100.0%), 302.00 (63.90%). Anal. calc. for $C_{17}H_{19}FN_2O$: C, 51.85, H, 2.68, N, 9.30. Found: C, 51.92, H, 2.75, N, 9.12.

TABLE 1 | Dimensions of the grid box of the proteins docked in this study.

Protein target	*X*	*Y*	*Z*
MAO-A (2Z5X)			
Center	40.6	26.85	−14.80
Dimensions (Å)	20.00	20.00	20.00
MAO-B (2BYB)			
Center	52.56	156.3	26.1
Dimensions (Å)	20.00	20.00	20.00

2.4 | Single Crystal X-Ray Crystallography

The appropriate crystal of FCF used for the single x-ray crystal elucidation was obtained by gradual evaporation of dichloromethane solution of FCF in one week. A suitable crystal with dimension 0.303 × 0.250 × 0.092 was mounted on a Bruker APEX II DUO CCD diffractometer with radiation (0.71073 Å) at a temperature of 100 K. The structure of FCF was solved and refined by exploring SHELXT [18] within the X-Seed environment [19]. Structural parameters together with structural data are presented in Table S1.

2.5 | Molecular Docking

The chain A of human MAO-A (PDB: 2Z5X) [20] and human MAO-B (PDB: 2BYB) [21] were extracted from the RCSB protein databank using Maestro 12.8 from the Schrodinger Suite. The proteins were preprocessed with the Protein Preparation Wizard, including bond order assignment, hydrogen addition, and setting protonated states at pH 7.0 ± 2.0 using Epik mode [22]. Subsequently, FCF and the reference drug for MAO-A, harmine (CID: 5280953), and that for MAO-B, rasagiline (CID: 3052776) obtained from PubChem were prepared with the LigPrep wizard of the Suite using the OPLS4 Force Field [23]. The receptor grid parameters were set using the parameters in Table 1, and docking was done using Glide [24]. Discovery Studio 2024 Client analyzed the protein–ligand interactions.

2.6 | Molecular Dynamics Simulation of the Best Ligand Candidate and the Receptors

FCF and reference drug complexes were prepared for molecular dynamics simulation (MDS) using Amber 18 GPU and FF18SB force field [25]. Ligand partial charges were generated with ANTECHAMBER using GAFF [26], and the restrained electrostatic potential (RESP) algorithms. To neutralize the systems, protein hydrogen atoms and counter ions (Cl^-, Na^+) were added via LeaP, and the system was soaked with TIP3P water in an octahedral case extending 8 Å from the proteins. The systems underwent 1000 steps each of steepest descent and conjugate gradient minimization. Proteins were fixed using 500 kcal mol^{-1} $Å^{-2}$ restraints. After heating to 300 K for 50 ps (NVT, 10 kcal mol^{-1} $Å^{-2}$ restraints), the system was equilibrated at 300 K for 500 ps (NPT, 1 atm pressure, 2 ps relaxation). Temperature was maintained with Langevin dynamics [27] with a collision frequency of 1 ps^{-1}. The total simulation time was 100 ns with a 2 fs step. Results were evaluated using CPPTRAJ in AMBER18.

2.7 | Validation of MDS

The AMBER 18 package using the CPPTRAJ script was used to analyze the root mean square deviation (RMSD) of the protein–ligand complexes and the ligands in the binding pocket, the radius of gyration (RoG), and root mean square fluctuation (RMSF). The raw data obtained were analyzed and plotted using the OriginPro software [28].

2.8 | Binding Free Energy Calculations

The molecular mechanics/Poisson–Boltzmann surface area (MM/PBSA) method was used to calculate and compare the binding affinity of protein–ligand complexes. Binding free energy was averaged over 100 000 snapshots from a 100 ns trajectory. The computed free binding energy (G) for each molecular species (complex, ligand, and receptor) is represented as follows:

$$\Delta G_{\text{bind}} = G_{\text{complex}} - G_{\text{receptor}} - G_{\text{ligand}} \quad (1)$$

$$\Delta G_{\text{bind}} = \Delta E_{\text{gas}} + \Delta G_{\text{sol}} - T\Delta S \quad (2)$$

$$\Delta E_{\text{gas}} = \Delta E_{\text{int}} + \Delta E_{\text{Van der Waals}} + \Delta E_{\text{elec}} \quad (3)$$

$$\Delta G_{\text{sol}} = \Delta G_{\text{GB}} + \Delta G_{\text{SA}} \quad (4)$$

$$\Delta G_{\text{SA}} = \gamma \text{SASA} \quad (5)$$

where E_{gas} is the gas-phase energy of the system, E_{int} is the internal energy within the molecular system, E_{elec} is the electrostatic energy from charged atomic interactions, $E_{\text{Van der Waals}}$ is the energy from Van der Waals interactions, G_{sol} is the solvation-free energy, G_{GB} is the polar contribution to solvation-free energy, G_{SA} is the nonpolar contribution to solvation-free energy, SASA is the solvent-accessible surface area, used to calculate hydrophobic solvation energy, S is the total entropy, representing the system's disorder, T is the temperature of the solute.

2.9 | Density Functional Theory Computational studies

The geometry optimization of FCF was conducted employing density functional theory (DFT) with the B3LYP hybrid functional [29, 30], utilizing the Gaussian 16 software package [31]. All calculations were executed on the Lengau cluster at the Centre for High Performance Computing (CHPC, Cape Town, South Africa; www.chpc.ac.za). The 6-311++G(d,p) basis set was employed for carbon (C), hydrogen (H), nitrogen (N), fluorine (F), and chlorine (Cl) atoms to ensure accurate electronic structure representation. Initial molecular configurations were constructed and visualized using the GaussView 6.0.16 interface [32], which also facilitated post-optimization structural analysis. To confirm the attainment of a true energy minimum on the potential energy surface, vibrational frequency calculations were performed, verifying the absence of imaginary frequencies.

Mulliken charge analysis [33] was subsequently applied to quantify atomic charge distributions within the optimized FCF

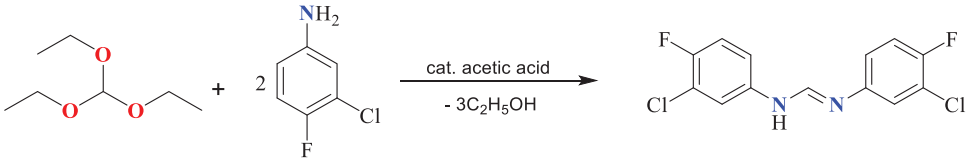

SCHEME 1 | *N,N′*-bis(3-chloro-4-fluorophenyl)formamidine (FCF).

structure. In addition, the molecular electrostatic potential (MESP) map was generated to evaluate reactivity trends, with color gradients delineating regions of varying electrostatic potential: blue (maximum positive potential, nucleophilic affinity), green (neutral), and red (maximum negative potential, electrophilic preference) [34, 35].

Frontier molecular orbital (FMO) analysis was carried out to elucidate electronic and reactive characteristics. Key parameters, including the energies of the highest occupied molecular orbital (HOMO), lowest unoccupied molecular orbital (LUMO), and the HOMO–LUMO energy gap (ΔE), were computed to assess charge transfer tendencies. The HOMO energy, correlating with ionization potential, reflects electron-donating capacity, while the LUMO energy signifies electron-accepting propensity. A reduced ΔE value implies heightened chemical reactivity and diminished kinetic stability [36–38].

Furthermore, global reactivity descriptors including the global hardness (η), global softness (σ), electronegativity (χ), and electrophilicity index (ω) were derived to quantify the molecule's stability and reactivity. These descriptors calculated using established relationships [39–41], provide insights into electron density resistance (η, σ), electron-attracting ability (χ), and nucleophilic interaction propensity (ω). The equations governing these descriptors are detailed in prior theoretical frameworks [39, 42], and given in Equations (6)–(9).

$$\eta = \frac{E_L - E_H}{2} \tag{6}$$

$$\sigma = \frac{1}{\eta} \tag{7}$$

$$\chi = \frac{-(E_H + E_L)}{2} \tag{8}$$

$$\omega = \frac{\mu^2}{2\eta} \tag{9}$$

The energies of the LUMO (E_L) and HOMO (E_H) are expressed in electronvolts (eV). These parameters offer valuable insights into the molecular behavior of FCF. The 3D structures were visualized using Chemcraft software [43], and the correlation analysis plot were illustrated using Origin software [44].

3 | Results and Discussion

3.1 | Synthesis of FCF

The synthetic route for the preparation of FCF is given in Scheme 1 and this was carried out by reacting two equivalents of 3-chloro-4-fluoroaniline and one equivalent of triethyl orthoformate under suitable reaction conditions as detailed in Section 2.1. The compound FCF is obtained in good yield (77%) and very stable at room temperature. FCF readily dissolves in chloroform, dimethyl sulfoxide, dichloromethane, dimethylformamide, toluene, partially soluble in ethanol but insoluble in hexane.

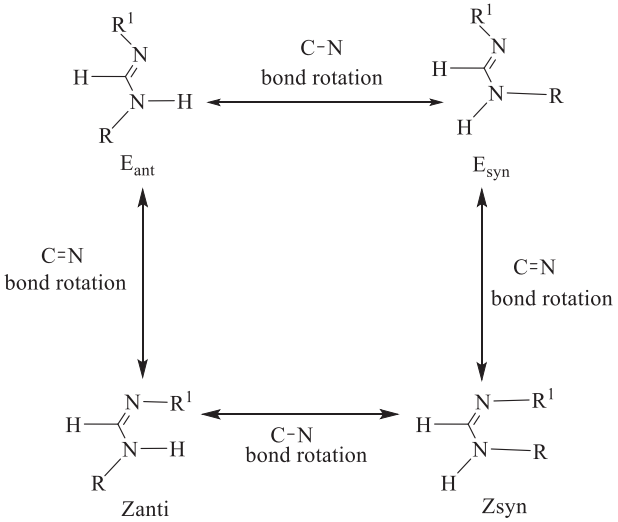

SCHEME 2 | Possible four isomers of formamidines in solution [45].

3.2 | Spectroscopic Elucidation

3.2.1 | ^{1}H and ^{13}C NMR

The NMR spectra (^{1}H and ^{13}C) of FCF were recorded in deuterated dimethyl sulfoxide, using 2D NMR for the assignment of peaks. Reports have shown that formamidines exist as four isomers in solution (Scheme 2), resulting in complex, poor resolution and in most cases inaccurate NMR spectra [45, 46].

Herein, we are able to account for all the protons in ^{1}H NMR spectrum of FCF, though the resolution is poor (Figure S1) despite using the 600 MHz spectrometer and the analysis carried out for a longer duration. The azomethine proton (—CH=N) appeared at 8.30 ppm while the one for secondary amine proton (—NH-Ar) appeared around 9.97 ppm as a broad peak. The peaks for the aromatic protons perfectly match and integrated well for FCF structure. These aromatic protons appeared around 7.15 ppm (2H) and 7.35 ppm (4H) as singlet and triplet, respectively. As regards the ^{13}C NMR spectrum for FCF, the diagnostic azomethine carbon (—CH=N) appeared around 160.35 ppm and the ones for aromatic carbons appeared within the range of 117.35–154.42 ppm

(Figure S2). These values are similar to those for similar structures reported in literature [13, 47, 48].

3.2.2 | FT-IR and Mass Spectra Analysis

In the FT-IR spectrum of FCF, major diagnostic peaks observed are formamidinyl C—H, N—H (secondary amine) and azomethine C═Nstr vibrational mode. The formamidinyl C—H peak appeared around 3078 cm^{-1} while the one for N—H was observed around 3100–3200 cm^{-1} and of very low intensity. The azomethine C═Nstr peak appeared around 1664 cm^{-1} (Figure S3) and this value is similar to those of formamidine derivatives reported in literature [47, 49]. Other notable peaks observed are C═Cstr of the aromatic moiety in FCF and C—Nstr and these appeared at 1589 and 1258 cm^{-1}, respectively. The vibrational band of C—X bond, that is, C—F and C—Cl also appeared in the spectrum of FCF within the range of 886–689 cm^{-1}.

The $[M]^+$, $[M+2]^+$, and $[M+4]^+$ peaks were observed in the mass spectrum of FCF and it appeared at 301.0109, 303.0081, and 305.0064, respectively (Figure S4). The intensity of the $[M]^+$, $[M+2]^+$, and $[M+4]^+$ peaks are in the ratio of 9:6:1 which is an attribute of organic molecule with two chlorine atoms [50, 51].

3.3 | Single Crystal x-Ray Description

The symmetrical formamidine FCF crystallizes as triclinic with space group of *P*-1 and in its asymmetric unit, it consists only one molecule of FCF (Figure 1a). In the solid state, FCF displays a trans geometry about the C═N double bond and exhibits E_{anti} isomerism (anti-conformation) about the C(H)—N(H) single bond. This is similar to the co-crystal of (*E*)-*N*,*N*′-bis(2,6-dichlorophenyl)formimidamide reported by Zamisa et al. [49] The dihedral angle between the plane of the two phenyl rings in FCF is 78.01° and this seems broader when compared to the one for E_{anti} of symmetrical (*E*)-*N*,*N*′-bis(2,6-dichlorophenyl)formimidamide which is 50.26° [49]. The dihedral angles between the two phenyl rings and the —N(2)═C(7)—N(1)— moiety which are C8—N2—C7—N1 and C5—N1—C7—N2 are 173.42° and 168.58°, respectively. This depicts that one of the phenyl rings is more coplanar with the —N(2)═C(7)—N(1)— moiety than the other. The C8—N2, C7—N2, C7—N1, and C5—N1 bond distances are 1.421, 1.290, 1.353, and 1.409 Å, respectively, depicting the availability of single and double bonds between carbon and nitrogen atoms linking the two phenyl rings in FCF. Figure 1b, represents the crystal packing diagram of FCF. There are four molecules per unit cell which are strongly connected through hydrogen bonding to form dimers with about 2.130 Å distance between the two molecules.

The classical N—H···N hydrogen bonding intermolecular interaction was observed in the crystal packing of FCF and this is peculiar to all *N*,*N*′-diphenylformamidines [52, 53]. It was formed between the azomethine nitrogen (N-azomethine) and amine hydrogen (H-amine) atoms resulting into the formation of dimers with a $R_2^2(8)$ graph set motif [52]. Besides N—H···N interaction, C—H···F and C—H···Cl intermolecular interactions also exist in the packing system of FCF. The geometric parameters

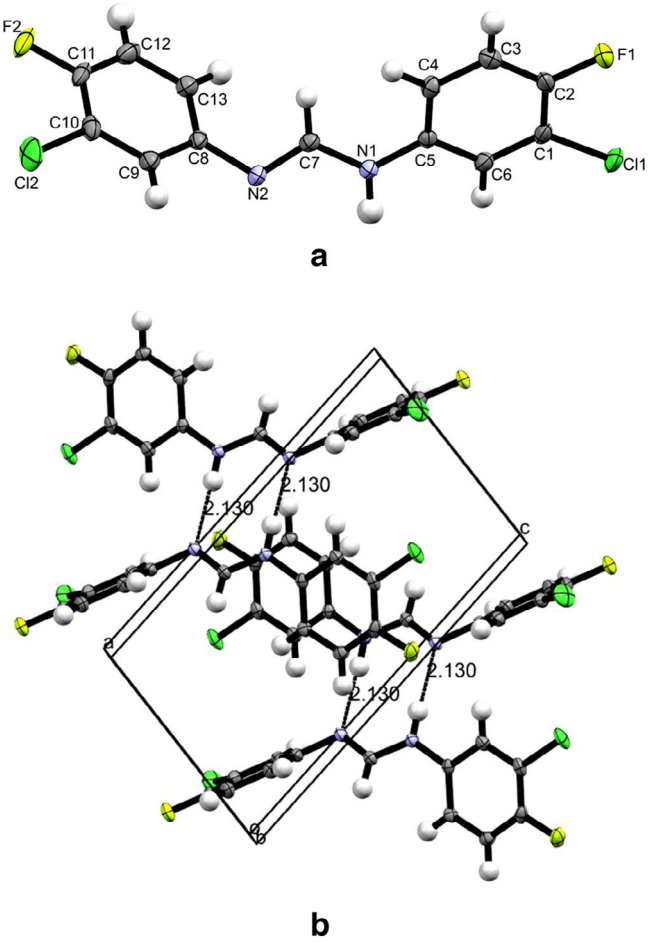

FIGURE 1 | (a) Crystal structure of FCF with thermal ellipsoids drawn at 60% probability. Hydrogen atoms have been omitted for clarity. (b) Diagram showing intermolecular N1—H1···N2 hydrogen bonding existing in the packing diagram of FCF.

of the intermolecular C—H···F, C—H···Cl, and N—H···N hydrogen bonds are summarized in Table 2.

3.4 | Hirshfeld Surface Analysis of FCF

Hirshfeld surface (HS) analysis helps to provide crucial information about surface characteristics of molecules and reveal the molecular interaction existing in their crystal packing systems [54, 55]. HS analysis (HSA) unravels the nature of interactions as well, either weak or strong in crystal packing of molecules. It could be defined as the points where the contribution to electron density inside the surface of a molecule is equal to the ones from all other molecules in the crystal packing [56]. The *CrystalExplorer21* [57] software was used to generate the Hirshfeld surface of FCF, mapped with d_{norm} function together with the 2D fingerprint plots of significant intermolecular interactions (Figure 2). On the d_{norm} surface, crucial information about the surface characteristics is encoded with red, blue, and white region. The red region signifies closer contacts with negative d_{norm} value, that is, sum of Van der Waal radii longer than distance of contact while blue region signifies longer contact with positive d_{norm}, that is, sum of Van der Waals radii shorter than distance

TABLE 2 | Hydrogen-bond geometry (Å°) parameter for FCF.

D—H···*A*	*D*—H	H···*A*	*D*···*A*	*D*—H···*A*
N1—H1···N2^{i}	0.900 (18)	2.129 (19)	3.0268 (15)	176.0 (15)
C9—H9···F1^{ii}	0.95	2.48	3.3809 (15)	158
C3—H3···F1^{iii}	0.95	2.60	3.2018 (15)	122
C12—H12···Cl1^{iv}	0.95	2.84	3.7544 (14)	161

Note: Symmetry codes: (i) $-x+2, -y+1, -z+1$; (ii) $-x+1, -y+1, -z+1$; (iii) $-x, -y+2, -z+1$; (iv) $x+1, y, z-1$.

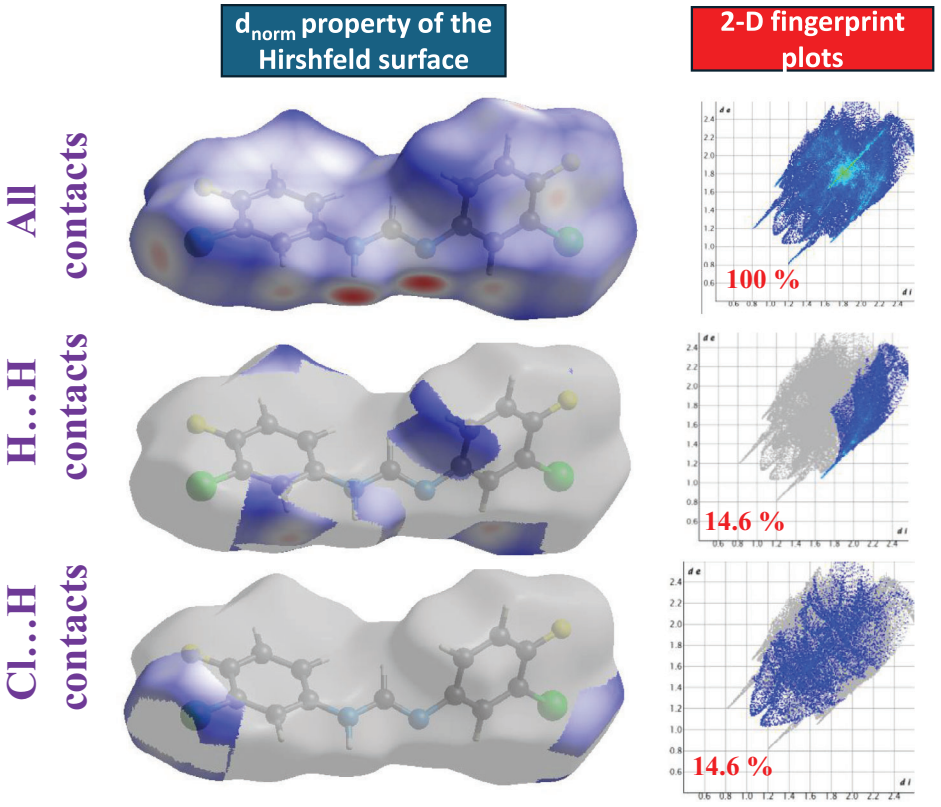

FIGURE 2 | D_{norm} property mapped over the HS and 2D fingerprint plots of the selected intermolecular interactions with their contribution towards the HS of FCF.

of contact. The white color depicts zero d_{norm} value, that is, the distance of contacts is approximated to the sum of Van der Waals separation [56, 58]. Short intermolecular interactions play a significant role in the stabilization of the crystal lattice; thus, this section majorly focuses on it. Interestingly, two intermolecular contacts contributed the most and equally towards the HS of FCF. These are H···H and Cl···H contacts and each of them contributed 14.6%. Significant quantity of hydrogen bonds was also observed, that is, H···F/F···H (9.4% F···H and 8.9% H···F) and N···H/H···N (3.2% N···H and 2.6% H···N) intermolecular contacts. It is important to note that, the circular deep red color observed on the d_{norm} surface of FCF is due to hydrogen bonding contacts (N···H/H···N) and could be clearly seen on 2D fingerprint plots as two elongated narrow spikes facing the bottom left (Figure 2). Some other notable intermolecular contacts are H···Cl (9.7%), C···C (8.5%), C···H (5.6%), and H···C (4.4%). In the shape index of FCF (Figure S5), we observed an adjacent red and blue triangle on the HS, affirming the presence of $\pi\cdots\pi$ stacking interactions in the crystal packing system [56].

3.5 | Molecular Docking

3.5.1 | Binding Affinity

The molecular docking studies was carried out for FCF as well as reference drugs (harmine and rasagiline) against MAO-A (2Z5X), and MAO-B (2BYB) and their docking scores are presented in Table S2. The outcomes of the study revealed that, the docking scores for FCF outshined the one for the reference drugs. We further ran MDS analysis for the ligand–protein complexes of FCF and the one for reference drugs at 100 ns. This is to unravel the interaction between FCF and reference drug with MAO-A/MAO-B. Thus, revealing the inhibitory potential of FCF against MAO-A and MAO-B enzymes.

TABLE 3 | Thermodynamic ΔG_{bind} profiles for FCF and harmine/rasagiline with MAO-A and MAO-B.

Complexes	$E_{Van\ der\ Waals}$	E_{elec}	ΔG_{gas}	ΔG_{sol}	ΔG_{bind}
MAO-A					
Harmine–MAO-A	−36.1473 ± 2.2677	−13.7373 ± 2.5790	−49.8846 ± 2.8019	17.4504 ± 1.5151	−32.4341 ± 2.2625
FCF–MAO-A	−44.1816 ± 2.1126	−74.0197 ± 7.5789	−118.2013 ± 7.5995	79.4224 ± 6.6470	−38.7788 ± 2.6190
MAO-B					
Rasagiline–MAO-B	−32.2792 ± 2.2902	−28.6924 ± 8.5928	−60.9716 ± 8.7181	28.5244 ± 7.6553	−32.4472 ± 2.6529
FCF–MAO-B	−41.2829 ± 2.0969	−69.7349 ± 8.3712	−111.0177 ± 8.9970	76.8640 ± 6.9001	−34.1537 ± 3.2926

3.5.2 | MDS Studies

To evaluate the binding energies and affinities of FCF–protein complexes, MDS analysis was carried out [59]. The MM/PBSA method was explored to evaluate the binding free energies (ΔG_{bind}) between the ligand–protein/enzyme complexes [60]. The MDS analysis was carried out for 100 ns and thereafter, we estimated the binding energy of FCF and reference drugs at the active sites of proteins. Table 3 details the calculated binding free energies, and this could be used as a yardstick to measure the inhibitory potential of FCF against MAO-A and MAO-B enzymes and compare it to one for well-known drugs (harmine for MAO-A, rasagiline for MAO-B).

The FCF–MAO-A and harmine–MAO ligand–protein binding free energies (ΔG_{bind}) are −38.7788 ± 2.6190 and −32.4341 ± 2.2625 kcal mol^{-1}, respectively. These results show that FCF binds strongly with MAO-A when compared to harmine. This suggests that FCF could inhibit MAO-A better when compared to harmine (reference drug). The stronger binding free energies of FCF when compared to harmine can be attributed to stronger van der Waals interactions, electrostatic interaction and higher solvation-free energy.

In the case of MAO-B, FCF–MAO-B, and rasagiline–MAO-B binding free energies (ΔG_{bind}) are of −34.1537 ± 3.2926 and −32.4472 ± 2.6529 kcal mol^{-1}, respectively. These strong binding energies in both complexes are driven by high Van der Waals and electrostatic interactions. However, FCF–MAO-B binding energies outshined the one for rasagiline–MAO-B. The higher binding free energy in FCF can be attributed to much stronger Van der Waals and electrostatic interactions. Generally, FCF demonstrates stronger binding profiles for both MAO-A and MAO-B compared to the reference drugs (harmine and rasagiline). This indicates that, FCF could serve as a more potent therapeutic agent for targeting MAO-A and MAO-B due to their promising inhibitory potential against these enzymes. Hence, their possibility to improve the management of Parkinson's and other neurodegenerative diseases caused by MAO-A and MAO-B enzymes.

3.5.3 | Protein–Ligand Interaction

The ligand–protein interaction plot for FCF is given in Figure S6. These plots give insights into the types of amino residues which interact with FCF and reference drugs at the protein binding pockets. In harmine–MAO-A complex, the hydrogen bond interactions were observed with PHE197 and TYR396 while harmine also interacts with LEU86, PHE97, VAL199, ILE314, ILE324, LEU326, and TYR396 through alkyl/π-alkyl bonds. Furthermore, π–π stacked interactions were observed with PHE197 and Van der Waals interactions through TYR58, VAL87, ILE169, ILE196, SER198, GLN204, CYS312, MET313, THR325, MET339, PHE341, and TYR433 were also observed.

The FCF–MAO-A complex displaced hydrogen bonds through the interactions with ARG40 and THR424 and the alkyl/π-alkyl bonds were also observed through the interactions with ILE12, VAL292, LYS294, PHE341, CYS395, MET434, and ALA437. The π–π stacked/π–π T-shaped bonds were with TRP386 and TYR396 while the Van der Waals interactions were with GLY11, GLY38, THR41, GLY55, GLY56, SER212, GLY432, and TYR433.

For rasagiline–MAO-B complex, the hydrogen bonds were observed through the interactions with amino acids such as ILE196, GLN204, and TYR433. The alkyl/π-alkyl bonds occur through the interactions with TYR58, LEU169, CYS170, ILE196, TYR324 among others. The π–π T-shaped bond was observed through interactions with TYR324, the π—sulfur bond with CYS170, π—cation bonds with TYR58 as well as TYR396 and the Van der Waals interactions with PHE166, TYR186, and LEU326 were also observed.

Finally, in FCF–MAO-B complex, the hydrogen bonds were noticed through the interactions between ILE197 and TYR324 with FCF. The alkyl/π-alkyl bonds occurred through the interaction of FCF with VAL80, LEU326, TYR433, and MET434. The π–π T-shaped/amide—π stacked bonds are with GLY55 and TYR396 interacting with FCF. The halogen bonds are with ARG40 and ILE197, π—cation bond with TYR58, π—sulfur bond with CYS395, unfavorable positive–positive interaction with LYS294 and Van der Waals interaction with GLY56.

3.5.4 | Ligand-Binding Effects on Proteins' Structural Stability

This study explores the structural and conformational changes influencing the biological activity of MAO-A and MAO-B by analyzing key structural parameters, including RMSD, RoG, and RMSF for protein–ligand complexes. These parameters provide insights into the stability, compactness, and flexibility of the complexes, as detailed in Figure 3 and Table 4. A lower RMSD value indicates greater structural stability while a lower RoG suggests a more compact conformation [61]. Similarly, RMSF

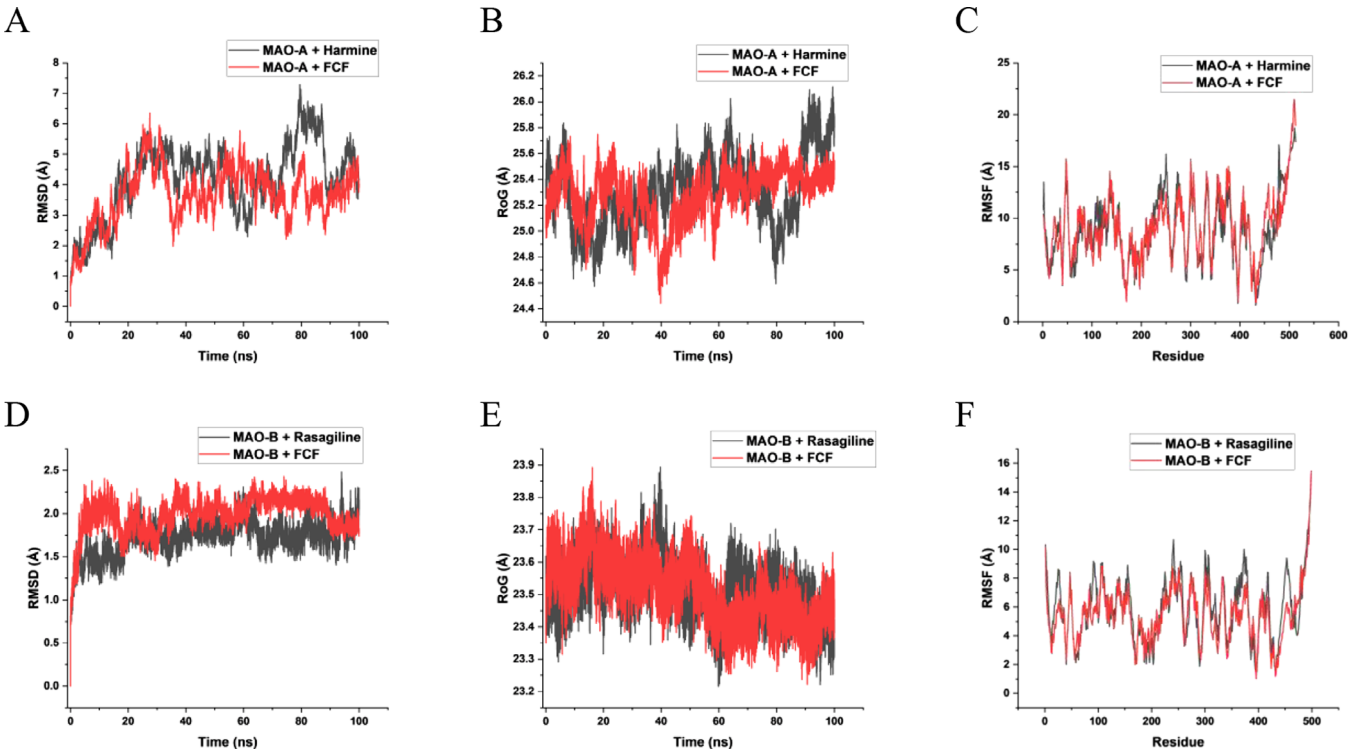

FIGURE 3 | Comparative RMSD, RoG, and RMSF plots of alpha C atoms in the monoamine oxidase systems, estimated over 100 ns of molecular dynamic simulations.

TABLE 4 | Calculated average values for RMSD, RoG, and RMSF for MAO-A and MAO-B complexes.

Ligand–protein complex	RMSD (Å), mean ± SD	RoG (Å), mean ± SD	RMSF (Å), mean ± SD
MAO-A + harmine	4.180 ± 1.187	25.308 ± 0.273	8.910 ± 3.299
MAO-A + FCF	3.673 ± 0.915	25.283 ± 0.201	9.156 ± 3.209
MAO-B + rasagiline	1.720 ± 0.197	23.513 ± 0.083	5.920 ± 2.208
MAO-B + FCF	1.984 ± 0.207	23.512 ± 0.096	5.472 ± 1.901

measures the flexibility of amino acid residues, with lower values reflecting reduced movement upon ligand binding [62].

For the MAO-A complexes, when MAO-A binds to harmine, the RMSD value is 4.180 ± 1.187 Å, the RoG is 25.308 ± 0.273 Å, and the RMSF is 8.910 ± 3.299 Å, indicating a relatively flexible structure. In contrast, the FCF–MAO-A complex exhibits a lower RMSD of 3.673 ± 0.915 Å, suggesting greater structural stability compared to the harmine-bound complex. The RoG value of 25.283 ± 0.201 Å is slightly lower than that of harmine, while the RMSF of 9.156 ± 3.209 Å indicates higher flexibility.

For the MAO-B complexes, the reference drug rasagiline demonstrates an RMSD of 1.720 ± 0.197 Å, RoG of 23.513 ± 0.083 Å, and RMSF of 5.920 ± 2.208 Å, signifying high stability and moderate flexibility. The FCF–MAO-B complex, however, shows a slightly higher RMSD of 1.984 ± 0.207 Å, indicating lower stability, but maintains a RoG of 23.512 ± 0.096 Å, suggesting a comparable compactness to rasagiline. In addition, its RMSF of 5.472 ± 1.901 Å reveals lower flexibility compared to the reference drug complex.

3.6 | Principal Component Analysis

Principal component analysis (PCA) is an effective technique for examining variance in molecular dynamics data of enzyme–ligand complexes. By converting the original dataset into a new coordinate system, PCA highlights key directions (principal components) that capture the most significant variations. This transformation simplifies complex datasets, making it easier to interpret molecular dynamics behavior [63]. This study applied PCA to examine the binding interactions of MAO-A and MAO-B complexes with FCF and a reference drug. Initially, RMSD values were collected and standardized using StandardScaler to ensure uniform feature contribution. PCA was then performed to reduce dimensionality while preserving variance, allowing for a clearer interpretation of structural dynamics during molecular simulations.

The results, summarized in Table 5 and Figure 4, reveal distinct variance patterns between MAO-A and MAO-B complexes. In MAO-A complexes, the first principal component (PC1) accounted for over 95% of the variance, with RMSD as the primary

TABLE 5 | PCA results for MAO-A and MAO-B complexes.

Complexes	Principal component	Eigenvalue	Explained variance (%)	RMSD loadings	RoG loadings
MAO-A–harmine	PC1	1.413524	95.24847	0.99857	−0.05339
	PC2	0.070515	4.75153	0.05338	0.99857
MAO-A–FCF	PC1	0.837418	95.41891	0.99999	−0.00257
	PC2	0.040205	4.581086	0.00256	0.99999
MAO-B–rasagiline	PC1	0.03934	86.13419	0.99093	−0.13435
	PC2	0.006333	13.86581	0.13435	0.990934
MAO-B–FCF	PC1	0.043631	83.89473	0.988535	−0.15099
	PC2	0.008376	16.10527	0.150989	0.988535

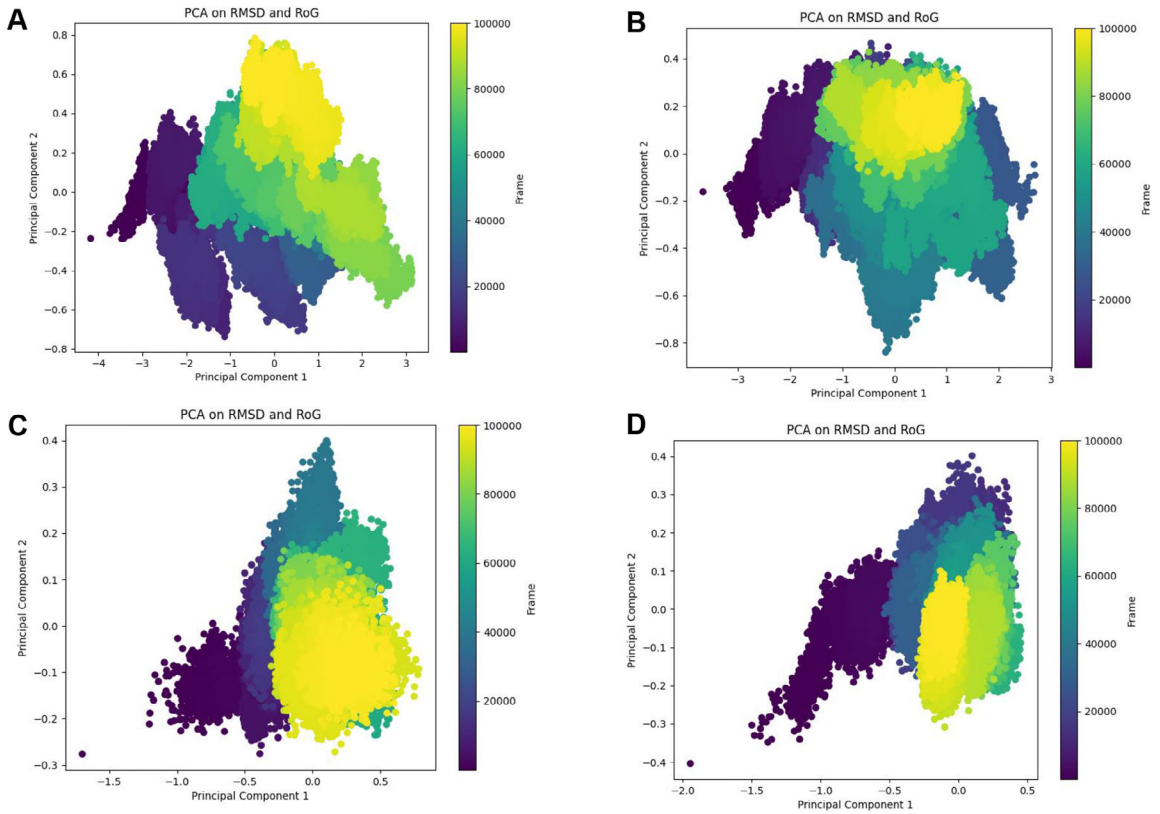

FIGURE 4 | Scatterplots of principal component analysis (PCA). Results for RMSD and RoG after 100 ns molecular dynamics simulation of (A) MAO-A–harmine, (B) MAO-A–FCF, (C) MAO-B–rasagiline, (D) MAO-B–FCF.

contributor, while RoG influenced PC2. For the MAO-A–harmine complex, PC1 explained 95.25% variance, and for the MAO-A–FCF complex, it captured 95.42% variance, following a similar trend.

In contrast, MAO-B complexes displayed a more evenly distributed variance between components. For the MAO-B–rasagiline complex, PC1 captured 86.13% of the variance, while for MAO-B–FCF, PC1 explained 83.89%, with RoG playing a more significant role in structural variation. Overall, MAO-A complexes showed a dominance of RMSD-driven variance, suggesting a consistent structural deviation pattern, whereas MAO-B complexes exhibited a more balanced contribution of RMSD and RoG, indicating more complex structural dynamics involving both deviations and compactness.

3.7 | Dynamic Cross-Correlation

Dynamic Cross-Correlation (DCC) analysis was conducted to examine the coordinated movements and dynamic interactions of protein residues within MAO-A and MAO-B complexes. This computational technique quantifies the degree of correlated motion between residue pairs, offering insights into the structural flexibility and functional mechanisms of protein–ligand

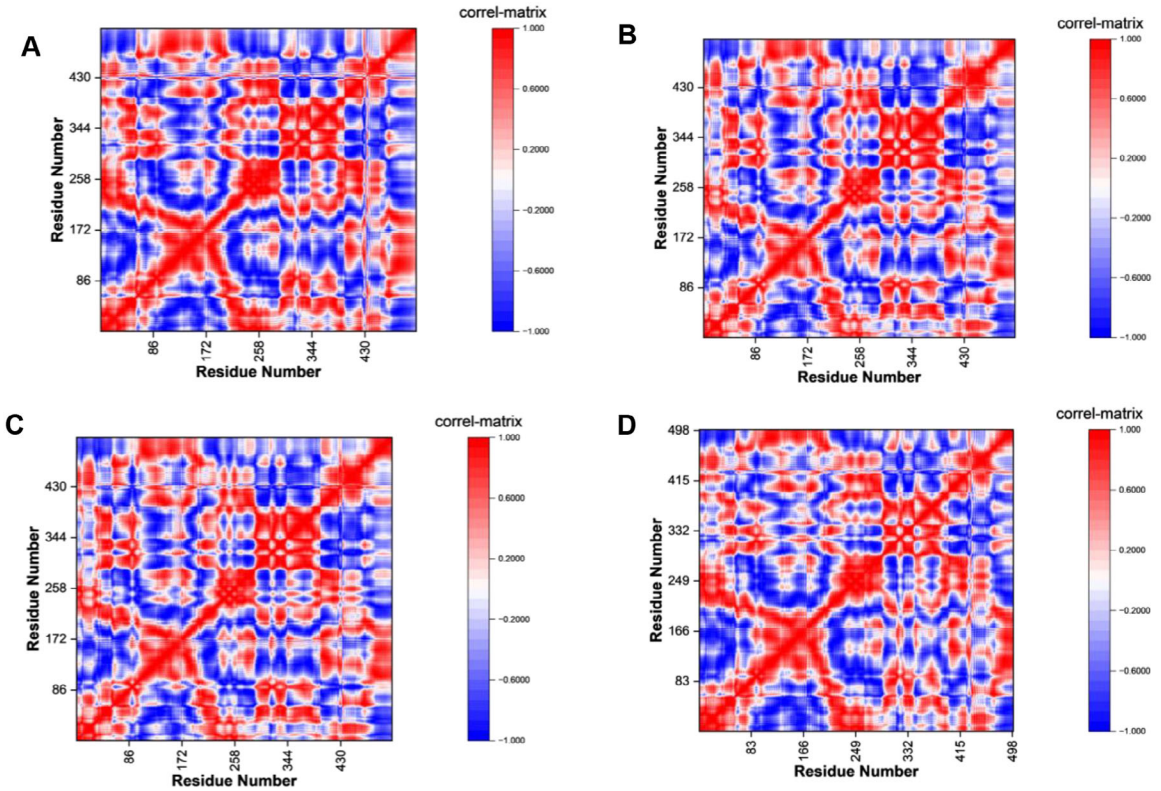

FIGURE 5 | Heatmaps of dynamic cross-correlation (DCC) analysis for: (A) MAO-A–harmine, (B) MAO-A–FCF, (C) MAO-B–rasagiline, (D) MAO-B–FCF.

interactions [64]. The results, illustrated in Figure 5, reveal how ligand binding influences protein dynamics and stability across different residue regions.

For the MAO-A–harmine complex, residues 1–86 displayed strong positive correlations, indicating a stable binding region, while a blue-to-red shift in residues 87–180 suggests conformational changes induced by harmine. A red-to-blue transition in residues 180–280 indicates altered dynamics due to ligand interaction, and residues 281–460 maintained strong positive correlations. A similar pattern was observed for the MAO-A–FCF complex, suggesting that FCF interacts with MAO-A similarly to harmine.

For the MAO-B–rasagiline complex, residues 1–86 exhibited strong positive correlations, signifying a stable ligand-binding region. A blue-to-red transition in residues 87–185 suggests that rasagiline enhances stability in previously flexible segments, while a red-to-blue shift in residues 186–280 indicates altered coordinated motions. Residues 281–460 maintained strong correlations, while regions beyond residue 460 displayed reduced coordinated movements. The DCC patterns for MAO-B–FCF closely mirrored those of rasagiline, implying similar effects on MAO-B dynamics.

These findings highlight the influence of ligand binding on protein flexibility and stability, with FCF exhibiting dynamic behavior similar to reference drugs (harmine and rasagiline). The correlated (red) and anti-correlated (blue) motions suggest that ligand interactions induce specific conformational changes within MAO proteins, affecting their binding properties. The conserved DCC patterns reinforce FCF's potential as a viable MAO inhibitor, and the distinct residue ranges (1–86, 87–180, 281–460) underscore critical regions for ligand recognition and binding affinity. These results provide valuable structural insights for rational drug design targeting MAO enzymes.

3.8 | Physicochemical and Pharmacokinetic Properties of FCF

SwissADME [65] and pkCSM [66] was utilized to estimate the physicochemical and pharmacokinetic properties of FCF and the results were summarized in Table S3. The compound complies with Lipinski's rule of five (Ro5), supporting its drug-like characteristics. With a molecular weight of 301.12 g mol^{-1} (below the 500 Da threshold) and a log*P* of 4.70 (within the acceptable lipophilicity limit), FCF exhibits good membrane permeability. Its log*S* value of −4.75 suggests moderate solubility, while a topological polar surface area (TPSA) of 24.39 $Å^2$ indicates high oral bioavailability. In addition, FCF has three hydrogen bond acceptors (HBA) and one hydrogen bond donor (HBD), aligning with drug-likeness criteria. The three rotatable bonds (RotBs) further ensure structural flexibility.

Pharmacokinetically, FCF demonstrates high gastrointestinal (GI) absorption, facilitating efficient oral uptake. Its ability to cross the blood–brain barrier (BBB) makes it suitable for central nervous system (CNS) applications. Importantly, FCF is not a substrate for P-glycoprotein (P-gp), suggesting a lower risk of drug efflux and improved brain bioavailability. With a logK_p of

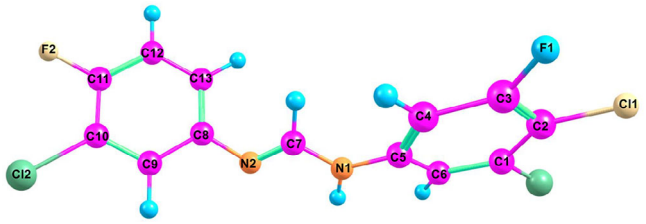

FIGURE 6 | The 3D structure of the FCF optimized at B3LYP/6-311++G(d,p) level of theory.

−5.01 cm s^{-1}, it exhibits moderate skin permeability. Toxicity assessments reveal no AMES toxicity or hepatotoxicity, indicating a favorable safety profile. The oral acute toxicity (LD_{50}) in rats is 2.704 mol kg^{-1}, and tetrahymena pyriformis toxicity (log μg L^{-1}) is 2.308, suggesting manageable toxicological risks. Overall, FCF possesses desirable physicochemical and pharmacokinetic properties, hence, a future potential candidate for the management of PD and other neurodegenerative disorders.

3.9 | DFT Computational Studies

3.9.1 | Geometry Optimization and Structural Analysis

The geometrical structure of FCF was optimized using DFT calculation at the B3LYP/6-311++G(d,p) level of theory. This hybrid functional and basis set was selected based on their demonstrated reliability in our prior studies for predicting structural parameters (bond lengths, bond angles, and dihedral angles) of formamidine derivatives, which showed strong agreement with experimental x-ray crystallographic data. The optimized structure (Figure 6) features a central amidino group, with the C7═N2 bond adopting a *trans* configuration relative to the N1—H bond. Both nitrogen atoms of the amidino group are substituted with phenyl rings, bearing chlorine and fluorine substituents at the 3- and 4-positions, respectively. These electron-withdrawing substituents induce electronic effects on the conjugation within the system. The *(E)*-configuration of the molecule positions the phenyl rings on opposite sides of the amidino plane, minimizing steric interactions and contributing to the stability of the molecule.

The theoretical bond lengths and angles, computed at the B3LYP/6-311++G(d,p) level, were compared with experimental values derived from x-ray crystallography, Figures 7 and 8 and Tables 6 and 7. The theoretical bond lengths show remarkable agreement with experimental data, with most differences being 0.02 Å or less (Table 6). For example, the bond lengths of C1—C6 (1.39 Å), C3—C2 (1.38 Å), and C5—C4 (1.40 Å) among others are identical in both methods, demonstrating the precision of the computational approach. Small deviations, such as in C1—Cl1 (1.73 vs. 1.74 Å), C10—Cl2 (1.73 vs. 1.75 Å), N1—C7 (1.35 vs. 1.37 Å), and N2—C8 (1.42 vs. 1.40 Å), may be due to challenges in modeling halogen interactions or electronic effects like resonance or conjugation that may not be fully captured by the functional. The C—F bonds, such as C2—F1 (1.36 vs. 1.35 Å), show excellent agreement, confirming that the basis set effectively models highly electronegative atoms like fluorine. In contrast, C—Cl bonds are slightly longer in the theoretical results, possibly due to weak dispersion forces or incomplete basis set descriptions for

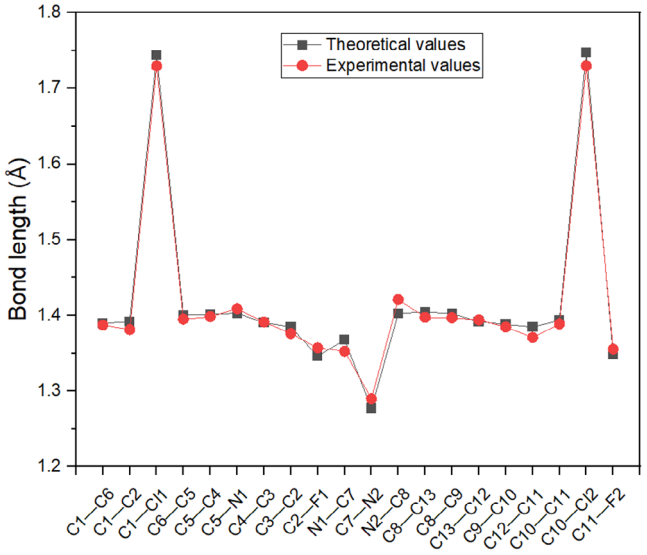

FIGURE 7 | Correlation plot of some experimental and theoretical bond lengths of FCF.

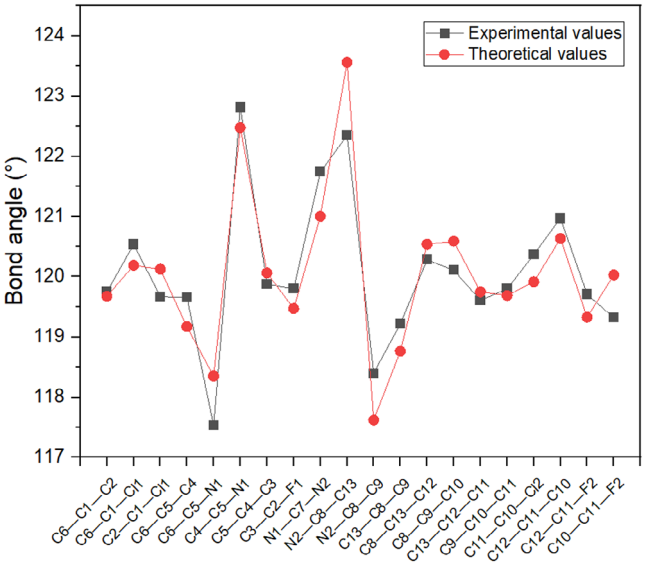

FIGURE 8 | Correlation plot of some experimental and theoretical bond angles of FCF.

chlorine atom. The uniformity of C—C bond lengths in the aromatic rings (e.g., C8—C13: 1.40 Å) suggests accurate modeling of the delocalized π-electron systems. Similarly, the C7═N2 bond (1.29 vs. 1.28 Å) shows a precise representation of double-bond character, which is essential for understanding conjugation in the molecule. Statistical analysis reveals a very high coefficient of determination (R^2 = 0.9944), indicating that the model explains more than 99% of the variance in the experimental bond lengths. The strong linear correlation (r = 0.9972) further supports the reliability of the B3LYP/6-311++G(d,p) method for studying the structure of similar organic molecules.

Table 7 and Figure 8 compare experimental bond angles of FCF (determined via x-ray crystallography) with theoretical values calculated at the B3LYP/6-311++G(d,p) level in the gas phase. The

TABLE 6 | Comparison of some experimental and theoretical bond length of FCF.

Bond length	Experimental values (Å)	Gas (Å)
C1—C6	1.39	1.39
C1—C2	1.38	1.39
C1—Cl1	1.73	1.74
C6—C5	1.40	1.40
C5—C4	1.40	1.40
C5—N1	1.41	1.40
C4—C3	1.39	1.39
C3—C2	1.38	1.38
C2—F1	1.36	1.35
N1—C7	1.35	1.37
C7═N2	1.29	1.28
N2—C8	1.42	1.40
C8—C13	1.40	1.40
C8—C9	1.40	1.40
C13—C12	1.39	1.39
C9—C10	1.38	1.39
C12—C11	1.37	1.38
C10—C11	1.39	1.39
C10—Cl2	1.73	1.75
C11—F2	1.36	1.35
Correlation coefficient r		0.9972
R^2 value		0.9944

TABLE 7 | Comparison of some experimental and theoretical bond angles of FCF.

Bond angle	Experimental values (°)	Gas (°)
C6—C1—C2	119.75	119.6792
C6—C1—Cl1	120.54	120.19
C2—C1—Cl1	119.67	120.1271
C1—C6—C5	119.91	120.4792
C6—C5—C4	119.66	119.1715
C6—C5—N1	117.53	118.3491
C4—C5—N1	122.81	122.4761
C5—C4—C3	119.88	120.0637
C4—C3—C2	119.63	120.1901
C1—C2—C3	121.16	120.3971
C1—C2—F1	119.05	120.1285
C3—C2—F1	119.8	119.4721
C5—N1—C7	124.14	127.0609
N1—C7═N2	121.74	121.0047
C7═N2—C8	115.77	119.5347
N2—C8—C13	122.35	123.5617
N2—C8—C9	118.4	117.6209
C13—C8—C9	119.22	118.7647
C8—C13—C12	120.28	120.5402
C8—C9—C10	120.11	120.5897
C13—C12—C11	119.61	119.7474
C9—C10—C11	119.8	119.6899
C9—C10—Cl2	119.83	120.3933
C11—C10—Cl2	120.37	119.9162
C12—C11—C10	120.97	120.6347
C12—C11—F2	119.71	119.328
C10—C11—F2	119.32	120.031
Correlation coefficient *r*		0.9099
R^2 value		0.8279

strong correlation between the datasets, evidenced by a correlation coefficient ($r = 0.9099$) and R^2 value (0.8279), confirms the reliability of the computational model in reproducing experimental geometries. Most angles deviate by less than 2°, demonstrating excellent agreement. For instance, the C6—C1—C2 angle (experimental: 119.75° vs. theoretical: 119.68°) and C5—C4—C3 angle (119.88° vs. 120.06°) show negligible differences, underscoring the method's precision in modeling carbon-carbon bond networks. Similarly, the C5—N1—C7 angle (124.14° vs. 127.06°) and N1—C7═N2 angle (121.74° vs. 121.00°) align closely, validating the accuracy of the computational approach for the molecule's central amidino functional group.

Larger deviations are observed in select cases, such as the C7═N2—C8 angle (experimental: 115.77° vs. theoretical: 119.53°), which differs by ∼3.7°. These discrepancies likely arise from electronic effects induced by electronegative substituents (e.g., chlorine and fluorine) or differences between gas-phase simulations (no intermolecular interactions) and solid-state experimental conditions. Angles involving fluorine substituents, such as C1—C2—F1 (119.05° vs. 120.13°), exhibit slight mismatches, potentially due to the computational model underestimating polarization effects caused by fluorine's electron-withdrawing nature in the crystalline environment. Minor variations, such as the C8—C13—C12 angle (120.28° vs. 120.54°), may reflect crystal-packing forces present in experimental measurements but absent in gas-phase calculations. These differences highlight inherent challenges in reconciling theoretical models (isolated molecules) with experimental solid-state data.

To sum up, the high consistency between theory and experiment underscores the suitability of the B3LYP/6-311++G(d,p) method for modeling FCF's geometry. While small deviations emphasize the limitations of comparing gas-phase simulations to crystal structures, the robust agreement supports the use of this computational approach for predicting structural, electronic, and reactive properties of FCF and related compounds.

Mulliken population analysis provides critical insights into molecular electron density distribution by assigning atomic charges through evaluation of electronic structures, bond param-

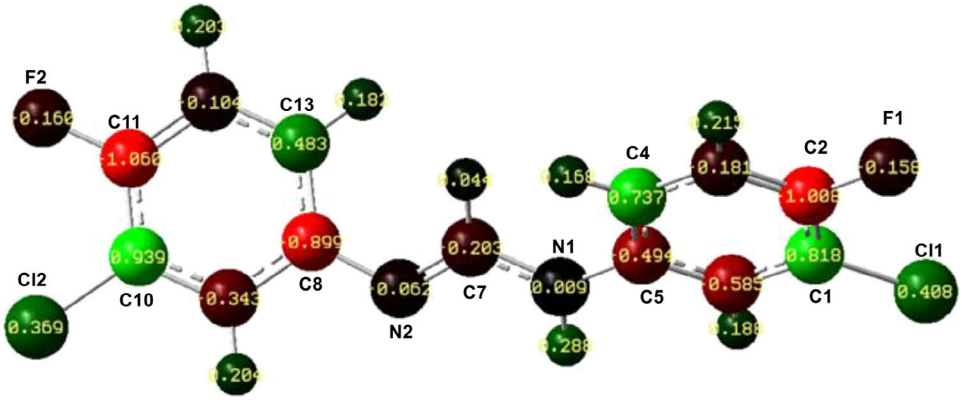

FIGURE 9 | Mulliken charge analysis of FCF at B3LYP/6-311++G(d,p) level of theory.

eters, dipole moments, polarizability, electrostatic potential surfaces, and bonding interactions [67]. As illustrated in Figure 9 for the fluorinated compound FCF, this method reveals distinct charge distributions that correlate with reactivity trends. Notably, the carbon atom (C11) bonded to the electronegative F group exhibits the highest negative charge (−1.06e), identifying it as a probable site for electrophilic interaction. Conversely, C10 emerges as the most electropositive atom (0.939e), attributed to the electron-withdrawing influence of the adjacent Cl substituent, rendering it susceptible to nucleophilic attack.

Intriguingly, the nitrogen centers in FCF display divergent charge characteristics: N1 bears a slight positive charge (0.009e), while N2 is moderately electronegative (−0.062e). This disparity arises from their distinct hybridization states and electronic environments. N2, adopting sp^2 hybridization with greater s-character, engages in π-delocalization via the C═N bond, enhancing electron deficiency through resonance effects. In contrast, N1, with sp^3 hybridization, retains higher electron density due to reduced participation in π-bonding or resonance, thereby diminishing its electronegativity. These findings underscore the utility of Mulliken analysis in elucidating electronic structure-reactivity relationships in complex molecular systems.

3.9.2 | MESP

MESP analysis represents a powerful methodology for elucidating the reactivity of molecules by mapping regions prone to nucleophilic and electrophilic interactions [68]. This approach provides atomic-level insights into intermolecular interactions, including hydrogen bonding, which are pivotal for predicting macroscopic behaviors such as solubility, chemical reactivity, and bioactivity [69]. MESP visualization facilitates the spatial identification of electron-rich and electron-deficient zones: negative electrostatic potentials (typically rendered in red/yellow hues) correspond to sites of elevated electron density, favoring electrophilic attack, while positive potentials (depicted in blue) denote electron-deficient regions susceptible to nucleophilic interactions.

For FCF, the MESP surface (Figure 10) demonstrates distinct electrostatic features. A pronounced yellow region localizes around the fluorine atom, while a yellowish-green zone is evident around the chlorine atom, indicative of higher electron

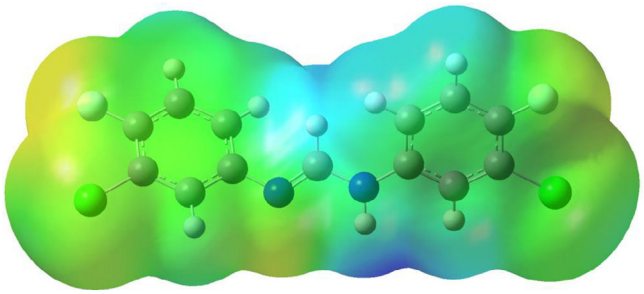

FIGURE 10 | MESP map of FCF in gas phase at B3LYP/6-311++G(d,p) level of theory.

density at the fluoride ion compared to the chloride moiety. This aligns with Mulliken charge analysis, which corroborates the greater electronegativity of the fluoride ion relative to chloride. Conversely, blue and light-blue regions, associated with reduced electron density, dominate hydrogen atoms and the N—H bond environment, marking these as electrophilic regions vulnerable to nucleophilic attack. The phenyl rings exhibit a uniform green coloration, signifying regions of neutral electrostatic potential.

3.9.3 | FMO Analysis and Quantum Chemical Studies

FMO analysis offers critical insights into electron transfer dynamics between the HOMO and LUMO, elucidating the stability and reactivity profiles of chemical compounds [70]. For the compound FCF, FMO calculations were performed at the B3LYP/6-311++G(d,p) theoretical level. The results revealed distinct localization patterns: the LUMO electron density was concentrated mainly around the carbon atom (C7) of the amidino functional group, indicative of electrophilic character and a propensity to accept electrons from electron-rich nucleophiles. On the other hand, the HOMO density predominantly resides on the π-system of the phenyl fragments and on the C═N bond of the amidino group, suggesting susceptibility to electrophilic attack or π–π interactions with electron-deficient species (Figure 11).

The computed HOMO and LUMO energies for FCF were −6.27 and −1.65 eV, respectively, yielding an energy gap (ΔE) of 4.62 eV (Table 8). According to Koopman's theorem, these values correspond to an ionization potential (IP = 6.27 eV)

TABLE 8 | Quantum chemical descriptors of FCF.

Parameter	E_{LUMO} (eV)	E_{HOMO} (eV)	ΔE (eV)	EA (eV)	IP (eV)	η (eV)	σ (eV^{-1})	μ (eV)	χ ($eV^{1/2}$)	ω (eV)
FCF	−1.65	−6.27	4.62	1.65	6.27	2.31	0.43	−3.96	3.96	3.40

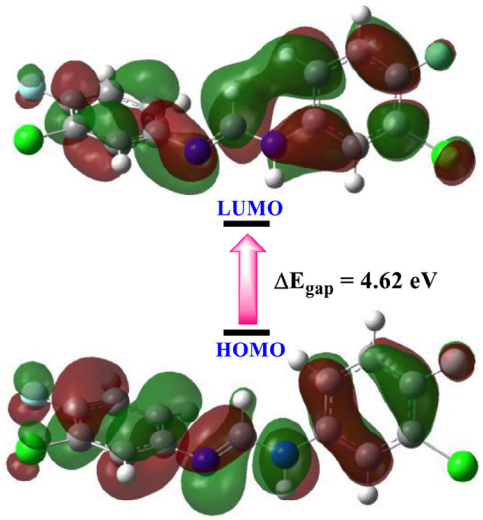

FIGURE 11 | The LUMO, HOMO, and HOMO–LUMO energy gap of FCF.

and electron affinity (EA = 1.65 eV) [71]. The relatively high EA and moderate IP imply that FCF exhibits pronounced electrophilic behavior. Furthermore, the ΔE value reflects intermediate chemical reactivity and stability, supported by derived global reactivity descriptors. Global hardness (η = 2.31 eV) and softness (σ = 0.43 eV^{-1}) values indicate high stability and low reactivity, consistent with the compound's electronic structure. Chemical potential (μ = 3.96 eV) and electrophilicity index (ω = 3.40 eV) were calculated to assess charge transfer trends and energy stabilization upon electron uptake. While high μ and ω values are often associated with nucleophilic tendencies [1], FCF's significant hardness and electronegativity (χ = 3.96 eV) emphasize its thermodynamic stability and electron-withdrawing capacity.

4 | Conclusion

Halogenated symmetrical formamidines, FCF was prepared successfully and elucidated by utilizing physicochemical and spectroscopic techniques. Single crystal spectroscopic analysis unravels FCF to conform to E_{anti} molecular isomer with dihedral angle 78.01° between the plane of the two phenyl rings in its structure. Two intermolecular contacts (H···H and Cl···H) contributed the most and equally (14.6% each) towards the HS of FCF. Quantum chemical calculations of FCF revealed their intermediate reactivity and stability. DFT studies showed strong agreement between experimental x-ray and theoretical data for bond lengths and angles (R^2 = 0.9944), with minor deviations attributed to solid-state effects. Our findings revealed FCF as a promising inhibitor of MAO-A and MAO-B, with molecular docking and MDS confirming its superior binding affinity and stability compared to the reference drugs harmine and rasagiline. The stronger binding free energies of FCF suggest its potential as a more effective therapeutic agent for PD. Furthermore, its favorable pharmacokinetic properties, including high GI absorption and BBB permeability, reinforce its potential for CNS applications. Despite these promising findings, future research should also focus on optimizing FCF's structural analogs to enhance its potency and selectivity. In addition, long-term toxicity and metabolic stability studies are necessary to evaluate its safety profile before clinical translation. Overall, these findings lay the groundwork for the continuous exploration of FCF as a viable candidate for PD management and treatment.

Author Contributions

Segun D. Oladipo: Conceptualization, methodology, software, validation, formal analysis, resources, data curation, writing original draft preparation, writing review and editing, visualization, funding acquisition, **Robert C. Luckay**: Conceptualization, methodology, software, validation, formal analysis, resources, data curation, writing original draft preparation, writing review and editing, visualization, supervision, project administration, funding acquisition, **Samuel O. Olalekan**: Conceptualization, methodology, software, validation, formal analysis, data curation, writing original draft preparation, writing review and editing, **Abosede A. Badeji**: methodology, software, validation, formal analysis, data curation, writing original draft preparation, writing review and editing, **Tunde L. Yusuf**: methodology, software, formal analysis, data curation, writing original draft preparation, writing review and editing, **Adesola A. Adeleke**: methodology, software, formal analysis, data curation, writing original draft preparation, writing review and editing, **Nonkosi Matinise**: methodology, software, formal analysis, data curation, writing original draft preparation, writing review and editing.

Acknowledgments

The authors acknowledge the funding from the National Research Foundation (grant number: CPRR23041794158), Stellenbosch University, Matieland, 7602, South Africa. The first author is a recipient of a postdoctoral fellowship award of the N.R.F. at Stellenbosch University, Matieland, South Africa. The authors are also grateful to the South African Centre for High-Performance Computing, CHPC (www.chpc.ac.za) for resources.

Conflicts of Interest

The authors declare no conflict of interest

Data Availability Statement

The data that support the findings of this study are openly available in Cambridge Crystallographic Data Centre at https://www.ccdc.cam.ac.uk/structures/search?Ccdcid=2423556&DatabaseToSearch=CSD, reference number 2423556.

References

1. A. B. R. Leite Silva, R. W. Gonçalves De Oliveira, and G. P. Diógenes, "Premotor, Nonmotor and Motor Symptoms of Parkinson's Disease: A New Clinical State of the Art," *Ageing Research Reviews* 84 (2023): 101834.

2. D. J. Kim, A. L. Isidro-Pérez, M. Doering, et al., "Prevalence and Incidence of Parkinson's Disease in Latin America: A Meta-Analysis," *Movement Disorders* 39 (2024): 105–118.

3. K. Śmiłowska, T. Pietrzykowski, A. J. Owczarek, E. R. Dorsey, B. R. Bloem, and D. J. van Wamelen, "The Prevalence of Parkinson's Disease in Poland: Regional and Sex-Related Differences," *Journal of Parkinson's Disease* 14 (2024): 521–532.

4. Z. Song, S. Liu, X. Li, et al., "Prevalence of Parkinson's Disease in Adults Aged 65 Years and Older in China: A Multicenter Population-Based Survey," *Neuroepidemiology* 56 (2022): 50–58.

5. X. Y. Chen, C. Liu, Y. Xue, and L. Chen, "Changed Firing Activity of Nigra Dopaminergic Neurons in Parkinson's Disease," *Neurochemistry International* 162 (2023): 105465.

6. N. Ebadpour, M. Mahmoudi, R. Kamal Kheder, et al., "From Mitochondrial Dysfunction to Neuroinflammation in Parkinson's Disease: Pathogenesis and Mitochondrial Therapeutic Approaches," *International Immunopharmacology* 142 (2024): 113015.

7. Y. Jinsmaa, V. R. Florang, J. N. Rees, et al., "Dopamine-Derived Biological Reactive Intermediates and Protein Modifications: Implications for Parkinson's Disease," *Chemico-Biological Interactions* 192 (2011): 118–121.

8. B. Mishal, A. Shetty, and P. Wadia, "Adverse Effects of Medications Used to Treat Motor Symptoms of Parkinson's Disease: A Narrative Review," *Annals of Movement Disorders* 6 (2023): 45–57.

9. D. Sengupta, A. Gómez-Torres, and S. Fortier, *Comprehensive Coordination Chemistry III*, 3th ed., (Elsevier, 2021), 366–405.

10. M. Rillich, L. Häussler, D. Jehnichen, and F. Böhme, "Polymers Containing Formamidine Groups," *Polymer Bulletin* 34 (1995): 43–48.

11. L. Anglada, M. Raga, M. Marquez, A. Sacristán, J. M. Castello, and J. A. Ortiz, "Synthesis and Assessment of Formamidines as New Histamine H2-receptor Antagonists," *Arzneimittel-Forschung* 47 (1997): 431–434.

12. P. D. Evans and J. D. Gee, "Action of Formamidine Pesticides on Octopamine Receptors," *Nature* 287 (1980): 60–62.

13. S. D. Oladipo, C. Mocktar, and B. Omondi, "*In Vitro* Biological Studies of Heteroleptic Ag(I) and Cu(I) Unsymmetrical *N*,*N*′-Diarylformamidine Dithiocarbamate Phosphine Complexes; the Effect of the Metal Center," *Arabian Journal of Chemistry* 13 (2020): 6379–6394.

14. S. D. Oladipo, B. Omondi, and C. Mocktar, "Co(III) *N*,*N*′-Diarylformamidine Dithiocarbamate Complexes: Synthesis, Characterization, Crystal Structures and Biological Studies," *Applied Organometallic Chemistry* 34 (2020): e5610.

15. S. D. Oladipo, B. Omondi, and C. Mocktar, "Synthesis and Structural Studies of Nickel(II)-and Copper(II)-*N*,*N*′-Diarylformamidine Dithiocarbamate Complexes as Antimicrobial and Antioxidant Agents," *Polyhedron* 170 (2019): 712–722.

16. H. J. Benezet and C. O. Knowles, "Further Studies of the Monoamine Oxidase Inhibiting Activity of Formanilides and Formamidines," *General Pharmacology* 11 (1980): 357–360.

17. B. A. Bailey R. J. Martin, and R. G. H. Downer, "Monoamine Oxidase Inhibition and Brain Catecholamine Levels in the Rat Following Treatment With Chlordimeform," *Pesticide Biochemistry and Physiology* 17 (1982): 293–300.

18. G. M. Sheldrick, "A Short History of SHELX," *Foundations of Crystallography* 64 (2008): 112–122.

19. L. J. Barbour, "X-Seed 4: Updates to a Program for Small-Molecule Supramolecular Crystallography," *Journal of Applied Crystallography* 53 (2020): 1141–1146.

20. S. Y. Son, J. Ma, Y. Kondou, M. Yoshimura, E. Yamashita, and T. Tsukihara, "Structure of Human Monoamine Oxidase A at 2.2-Å Resolution: The Control of Opening the Entry for Substrates/Inhibitors," *Proceedings of the National Academy of Sciences of the United States of America* 105 (2008): 5739–5744.

21. L. De Colibus, M. Li, C. Binda, A. Lustig, D. E. Edmondson, and A. Mattevi, "Three-Dimensional Structure of Human Monoamine Oxidase A (MAO A): Relation to the Structures of Rat MAO A and Human MAO B," *Proceedings of the National Academy of Sciences of the United States of America* 102 (2005): 12684–12689.

22. J. C. Shelley, A. Cholleti, L. L. Frye, J. R. Greenwood, M. R. Timlin, and M. Uchimaya, "Epik: A Software Program for pK_a Prediction and Protonation State Generation for Drug-Like Molecules," *Journal of Computer-Aided Molecular Design* 21 (2007): 681–691.

23. M. P. Jacobson, D. L. Pincus, C. S. Rapp, et al., "A Hierarchical Approach to All-Atom Protein Loop Prediction," *Proteins* 55 (2004): 351–367.

24. R. A. Friesner, J. L. Banks, R. B. Murphy, et al., "Glide: a New Approach for Rapid, Accurate Docking and Scoring. 1. Method and Assessment of Docking Accuracy," *Journal of Medicinal Chemistry* 47 (2004): 1739–1749.

25. P. C. Nair and J. O. Miners, "Molecular Dynamics Simulations: From Structure Function Relationships to Drug Discovery," *In Silico Pharmacology* 2 (2014): 4.

26. J. Wang, R. M. Wolf, J. W. Caldwell, P. A. Kollman, and D. A. Case, "Development and Testing of a General Amber Force Field," *Journal of Computational Chemistry* 25 (2004): 1157–1174.

27. R. J. Loncharich, B. R. Brooks, and R. W. Pastor, "Langevin Dynamics of Peptides: The Frictional Dependence of Isomerization Rates of *N*-Acetylalanyl-*N*′-Methylamide," *Biopolymers* 32 (1992): 523–535.

28. E. Seifert, "OriginPro 9.1: Scientific Data Analysis and Graphing Software—Software Review," *Journal of Chemical Information and Modeling* 54 (2014): 1552.

29. C. Lee, W. Yang, and R. G. Parr, "Development of the Colle-Salvetti Correlation-Energy Formula Into a Functional of the Electron Density," *Physical Review B* 37 (1988): 785–789.

30. Y. Zhao, N. E. Schultz, and D. G. Truhlar, "Exchange-Correlation Functional With Broad Accuracy for Metallic and Nonmetallic Compounds, Kinetics, and Noncovalent Interactions," *Journal of Chemical Physics* 123 (2005): 161103.

31. M. J. Frisch, G. W. Trucks, H. B. Schlegel, et al., *Gaussian 16 rev. 01* (2016), Wallingford, CT.

32. R. D. I. I. Dennington, T. A. Keith, and J. M. Millam, *GaussView, Version 6.0. 16* (Semichem Inc, 2016).

33. M. Franco-Pérez and J. L. Gázquez, "Electronegativities of Pauling and Mulliken in Density Functional Theory," *Journal of Physical Chemistry* 123 (2019): 10065–10071.

34. G. Ramesh and B. V. Reddy, "Barrier Potential, Structure (Monomer and Dimer), Inter-and Intra-Molecular Interactions, Vibrational Analysis, Fukui Functions, MESP, NBO, UV and NMR Analysis of Pyridine-3-Carboxylic Acid Using Spectroscopic and DFT Approach," *Polycyclic Aromatic Compounds* 43 (2023): 2488–2505.

35. A. A. Badeji, M. T. Omoniyi, T. B. Ogunbayo, S. D. Oladipo, and I. A. Akinbulu, "Quantum Chemical Investigation of the Degradation of Acid Orange 7 by Different Oxidants," *Discover Chemistry* 1 (2024): 55.

36. E. D. Akpan, S. D. Oladipo, T. W. Quadri, et al., "Formamidine-Based Thiuram Disulfides as Efficient Inhibitors of Acid Corrosion of Mild Steel: Electrochemical, Surface, and Density Functional Theory/Monte Carlo Simulation Studies," *ACS Omega* 7 (2022): 26076–26091.

37. A. A. Ogunlana, J. Zou, and X. Bao, "Insights Into the Mechanisms and Chemoselectivities of Carbamates and Amides in Reactions Involving Rh(II)-Azavinylcarbene: A Computational Study," *Journal of Organic Chemistry* 84 (2019): 8151–8159.

38. M. Miar, A. Shiroudi, K. Pourshamsian, A. R. Oliaey, and F. Hatamjafari, "Theoretical Investigations on the HOMO–LUMO Gap and Global Reactivity Descriptor Studies, Natural Bond Orbital, and Nucleus-Independent Chemical Shifts Analyses of 3-Phenylbenzo[*d*]Thiazole-2(3*H*)-Imine and Its *Para*-Substituted Derivatives: Solvent and Substituent Effects," *Journal of Chemical Research* 45 (2021): 147–158.

39. M. Karelson, V. S. Lobanov, and A. R. Katritzky, "Quantum-Chemical Descriptors in QSAR/QSPR Studies," *Chemical Reviews* 9 (1996): 1027–1044.

40. R. G. Parr, L. V. Szentpály, and S. Liu, "Electrophilicity Index," *Journal of the American Chemical Society* 121 (1999): 1922–1924.

41. S. D. Oladipo, S. J. Zamisa, A. A. Badeji, et al., "Ni^{2+} and Cu^{2+} Complexes of *N*-(2,6-Dichlorophenyl)-*N*-Mesityl Formamidine Dithiocarbamate Structural and Functional Properties as CYP3A4 Potential Substrates," *Scientific Reports* 13 (2023): 13414.

42. S. D. Oladipo, R. C. Luckay, K. A. Olofinsan, A. A. Badeji, and S. Mokoena, "Exploring Schiff Bases Derived From 4-(Diethylamino) Salicylaldehyde and Their Copper (II) Complexes as Antidiabetes and Antioxidant Agents: Structural Elucidation, DFT Computational and In Vitro Studies," *Inorganica Chimica Acta* 575 (2025): 122447.

43. G. A. Zhurko, Chemcraft, (2014), http://www.chemcraftprog.com.

44. E. Seifert, "OriginPro 9.1: Scientific Data Analysis and Graphing Software—Software Review," *Journal of Chemical Information and Modeling* (2014): 1552.

45. K. F. Kalz, A. Hausmann, S. Dechert, S. Meyer, M. John, and F. Meyer, "Solution Chemistry of *N*,*N*′-Disubstituted Amidines: Identification of Isomers and Evidence for Linear Dimer Formation," *Chemistry—A European Journal* 22 (2016): 18190–18196.

46. T. Elkin, N. V. Kulkarni, B. Tumanskii, M. Botoshansky, L. J. Shimon, and M. S. Eisen, "Synthesis and Structure of Group 4 Symmetric Amidinate Complexes and Their Reactivity in the Polymerization of α-Olefins," *Organometallics* 32, no. 21 (2013): 6337–6352.

47. S. D. Oladipo, F. A. Olotu, M. Soliman, C. Mocktar, and B. Omondi, "Formamidine-Based Thiuram Disulfides: Synthesis, Structural Characterization, Biological Studies, and Preliminary Cheminformatics Evaluation," *Journal of Molecular Structure* 1219 (2020): 128553.

48. S. D. Oladipo, G. F. Tolufashe, C. Mocktar, and B. Omondi, "Ag(I) Symmetrical *N*,*N*′-Diarylformamidine Dithiocarbamate PPh3 Complexes: Synthesis, Structural Characterization, Quantum Chemical Calculations and In Vitro Biological Studies," *Inorganica Chimica Acta* 520 (2021): 120316.

49. S. J. Zamisa, U. Bongoza, and B. Omondi, "Predicting Molecular Isomerism of Symmetrical and Unsymmetrical *N*,*N*′-Diphenyl Formamidines in the Solid-State: Crystal Structure, Hirshfeld Surface Analysis, Pairwise Interaction Energy, and ΔH_{fusion} and ΔS_{fusion} Correlations," *CrystEngComm* 23 (2021): 4459–4474.

50. S. D. Oladipo and R. C. Luckay, "Copper(II) Complexes Derived From Naphthalene-Based Halogenated Schiff Bases: Synthesis, Structural Analysis, DFT Computational Studies and In Vitro Biological Activities," *New Journal of Chemistry* 48 (2024): 13276–13288.

51. L. Ryan and R. Norris, *Cambridge International AS and A Level Chemistry Coursebook With CD-ROM* (Cambridge University Press, 2014).

52. M. K. Rofouei, N. Sohrabi, M. Shamsipur, E. Fereyduni, S. Ayyappan, and N. Sundaraganesan, "X-Ray Crystallography Characterization, Vibrational Spectroscopy, NMR Spectra and Quantum Chemical DFT/HF Study of *N*,*N*′-Di(2-Methoxyphenyl) Formamidine," *Spectrochimica Acta Part A, Molecular and Biomolecular Spectroscopy* 76 (2010): 182–190.

53. S. D. Oladipo, R. C. Luckay, A. A. Badeji, S. Z. Zamisa, S. O. Olalekan, and P. O. Oladoye, "Structural Studies, DFT Computational Analysis and Inhibitory Potential of (*E*)-*N*′-(2-Bromophenyl)-*N*-(2,6-Diisopropylphenyl) Formamidine Against CDK1 and CDK2," *Journal of Molecular Structure* 1320 (2025): 139734.

54. M. A. Spackman and D. Jayatilaka, "Hirshfeld Surface Analysis," *CrystEngComm* 11 (2009): 19–32.

55. S. D. Oladipo, T. L. Yusuf, S. J. Zamisa, et al., "Synthesis, Crystal Structure With Free Radical Scavenging Activity and Theoretical Studies of Schiff Bases Derived From 1-Naphthylamine, 2,6-Diisopropylaniline, and Substituted Benzaldehyde," *European Journal of Chemistry* 12 (2021): 204–215.

56. R. K. Mudsainiyan and S. K. Pandey, "A Combined Theoretical Calculation and Hirshfeld Surface Analysis of Cooperative Non-Covalent Interactions in the Crystal Packing in $[Cu(L1)_2(EDA)]$," *Zeitschrift für Anorganische und Allgemeine Chemie* 643, no. 20 (2017): 1245–1252.

57. P. R. Spackman, M. J. Turner, J. J. McKinnon, et al., "CrystalExplorer: A Program for Hirshfeld Surface Analysis, Visualization and Quantitative Analysis of Molecular Crystals," *Journal of Applied Crystallography* 54 (2021): 1006–1011.

58. S. D. Oladipo, R. C. Luckay, and K. A. Olofinsan, "Evaluating the Antidiabetes and Antioxidant Activities of Halogenated Schiff Bases Derived From 4-(Diethylamino) Salicylaldehyde: In Vitro Antidiabetes, Antioxidant and Computational Investigation," *Scientific Reports* 14 (2024): 27073.

59. S. O. Olalekan, V. A. Obakachi, A. A. Badeji, et al., "Exploring the Therapeutic Potential of Prolinamides as Multi-Targeted Agents for Alzheimer's Disease Treatment: Molecular Docking and Molecular Dynamic Simulation Studies," *In Silico Pharmacology* 12 (2024): 80.

60. M. Ylilauri and O. T. Pentikäinen, "MMGBSA as a Tool To Understand the Binding Affinities of Filamin–Peptide Interactions," *Journal of Chemical Information and Modeling* 53: 2626–2633.

61. S. D. Oladipo, O. I. Akinpelu, and B. Omondi, "Ligand-Guided Investigation of a Series of Formamidine-Based Thiuram Disulfides as Potential Dual-Inhibitors of COX-1and COX-2," *Chemistry & Biodiversity* 20 (2023): e202200875.

62. S. D. Oladipo, R. C. Luckay, K. A. Olofinsan, et al., "Antidiabetes and Antioxidant Potential of Schiff Bases Derived From 2-Naphthaldehye and Substituted Aromatic Amines: Synthesis, Crystal Structure, Hirshfeld Surface Analysis, Computational, and In Vitro Studies," *Heliyon* 10 (2024): e23174.

63. S. Kumar, R. Dubey, R. Mishra, et al., "Repurposing of SARS-CoV-2 Compounds Against Marburg Virus Using MD Simulation, Mm/GBSA, PCA Analysis, and Free Energy Landscape," *Journal of Biomolecular Structure & Dynamics* (2024): 1–20.

64. A. Kumar, A. Tiwari, and V. Tiwari, "Computational and Experimental Insights Into Glycyrrhizin-Loaded Nanostructured Lipid Carriers: Docking, Dynamics, Design Optimization, and Anticancer Efficacy in Lung Cancer Cells," *Future Journal of Pharmaceutical Sciences* 10 (2024): 164.

65. A. Daina, O. Michielin, and V. Zoete, "SwissADME: A Free Web Tool to Evaluate Pharmacokinetics, Drug-Likeness and Medicinal Chemistry Friendliness of Small Molecules," *Scientific Reports* 7 (2017): 42717.

66. D. E. Pires, T. L. Blundell, and D. B. Ascher, "pkCSM: Predicting Small-Molecule Pharmacokinetic and Toxicity Properties Using Graph-Based Signatures," *Journal of Medicinal Chemistry* 58 (2015): 4066–4072.

67. M. Arivazhagan, S. Manivel, S. Jeyavijayan, and R. Meenakshi, "Vibrational Spectroscopic (FTIR and FT-Raman), First-Order Hyperpolarizablity, HOMO, LUMO, NBO, Mulliken Charge Analyses of 2-Ethylimidazole Based on Hartree–Fock and DFT Calculations," *Spectrochimica Acta Part A, Molecular and Biomolecular Spectroscopy* 134 (2015): 493–501.

68. L. Liu, L. Miao, L. Li, et al., "Molecular Electrostatic Potential: A New Tool to Predict the Lithiation Process of Organic Battery Materials," *Journal of Physical Chemistry Letters* 9 (2018): 3573–3579.

69. M. A. Mumit, T. K. Pal, M. A. Alam, M. A. A. A. A. Islam, S. Paul, and M. C. Sheikh, "DFT Studies on Vibrational and Electronic Spectra, HOMO–LUMO, MEP, HOMA, NBO and Molecular Docking Analy-

sis of Benzyl-3-*N*-(2,4,5-Trimethoxyphenylmethylene) Hydrazinecarbodithioate," *Journal of Molecular Structure* 1220 (2020): 128715.

70. T. Chaudhary, M. K. Chaudhary, and B. D. Joshi, "Topological and Reactivity Descriptor of Carisoprodol From DFT and Molecular Docking Approach," *Journal of Institute of Science and Technology* 26 (2021): 74–82.

71. R. G. Parr and R. G. Pearson, "Absolute Hardness: Companion Parameter to Absolute Electronegativity," *Journal of the American Chemical Society* 105 (1983): 7512–7516.

Supporting Information

Additional supporting information can be found online in the Supporting Information section.

Supporting file 1: cbdv70128-sup-0001-SuppMat.pdf **Supporting file 2**: cbdv70128-sup-0002-SuppMat.cif